Applied Catalysis B: Environmental 205 (2017) 19–23

Contents lists available at ScienceDirect

Applied Catalysis B: Environmental

journal homepage: www.elsevier.com/locate/apcatb

Ultrathin graphitic C_3N_4 nanosheets as highly efficient metal-free cocatalyst for water oxidation

Chenchen Feng, Zhonghao Wang, Ying Ma, Yajun Zhang, Lei Wang, Yingpu Bi *

State Key Laboratory for Oxo Synthesis & Selective Oxidation, National Engineering Research Center for Fine Petrochemical Intermediates, Lanzhou Institute of Chemical Physics, CAS, Lanzhou, Gansu 730000, China

ARTICLE INFO

Article history:
Received 8 September 2016
Received in revised form
26 November 2016
Accepted 6 December 2016
Available online 7 December 2016

Keywords:
$BiVO_4$
Co-catalyst
Water oxidation

ABSTRACT

Here, we demonstrate that ultrathin graphitic-phase C_3N_4 nanosheets (g-C_3N_4-NS) could serve as an efficient metal-free cocatalyst for improving oxygen evolution activity on nanoporous $BiVO_4$ photoanode. More specifically, as compared with pure $BiVO_4$ photoanode, ultrathin g-C_3N_4 nanolayers not only suppress the surface charge recombination of $BiVO_4$, but also effectively transfer and store holes for water oxidation. As expected, the ultrathin graphitic-phase C_3N_4 cocatalyst modified $BiVO_4$ photoanode exhibited significantly improved photocurrent density and H_2 generation capability, nearly 7 and 12 times with respect to the pristine $BiVO_4$ under the same conditions. These results demonstrate an effective approach for the design and construction of low-cost and highly efficient PEC systems.

1. Introduction

Photoelectrochemical (PEC) water splitting is a potentially scalable approach to store solar energy in the form of clear and renewable H_2 fuel [1–4]. Among various semiconductors, *n*-type monoclinic bismuth vanadate ($BiVO_4$), with a moderate band gap matching well with solar spectrum, has recently emerged as a promising photoanode material for PEC water-splitting [5–13]. However, the PEC performance for water oxidation is far below that expected owing to the intrinsically sluggish kinetics of the oxygen evolution reaction (OER) dominated by photogenerated holes. In this regards, various strategies, including metal ions doping [14–17], hetero-coupling [18–21], and cocatalyst deposition [8–11,22,23], have been extensively employed to improve the performances of $BiVO_4$-based photoanodes. Particularly, depositing *p*-type VIII metal (Fe, Co, Ni) oxide or (oxy) hydroxide with reversible redox properties, which have been extensively utilized as electrocatalysts for water oxidation, has been proved to be a more effective approach to accelerate the surface charge separation as well as minimize the kinetic over potential [11,24,25]. More specifically, the photogenerated holes could be extracted from the $BiVO_4$ bulk and stored in the *p*-type cocatalysts for suppressing electron-hole recombination. Recently, Gong et al. [22] demonstrated that the loading *p*-Co_3O_4 particles on $BiVO_4$ photoanodes enables simultaneous enhancement of surface reaction kinetics and bulk charge separation. Gamelin et al. [15] modified W: $BiVO_4$ photoanode surfaces with Co-Pi catalyst, which yielded a large cathodic shift (~440 mV) in the onset potential for PEC water oxidation. Choi et al. [9–11] reported that the loading *p*-type FeOOH and NiOOH dual-layers onto $BiVO_4$ photoanodes could greatly improve the PEC performances. Domen et al. [23] reported that dual catalysts of CoO_x and NiO loaded $BiVO_4$ photoanodes enables a 1.5% half-cell solar-to-hydrogen efficiency for the water oxidation. Although these *p*-type VIII metal cocatalysts could effectively enhance the PEC properties of $BiVO_4$ photoanodes, but the metallic ions containing materials with perceptive toxicity definitely hampered their further applications. Moreover, their usual large thicknesses or dimensions may block sunlight absorption and prolong the holes transport distances. Thereby, the exploration of novel *p*-type metal-free co-catalysts with ultrathin structures may be an alternative strategy for enhancing the PEC performances of $BiVO_4$ photoanodes.

As a typical *p*-type metal-free semiconductor, graphitic-phase carbon nitride (g-C_3N_4) with a graphite-like layered structure has been extensively applied in photocatalytic hydrogen generation [26–29], degradation of organic pollutants [30–33], electrochemical sensors [34,35], and biomedical imaging [36], owing to its appropriate bandgap (2.7 eV), thermal and chemical stability, and nontoxic properties. However, the applications for water oxidation over g-C_3N_4 have been rarely reported as a result of its relatively low position of valence bands. Furthermore, the direct charge transfer across g-C_3N_4 layer is difficult as a result of the graphite-

* Corresponding author.
E-mail address: yingpubi@licp.cas.cn (Y. Bi).

http://dx.doi.org/10.1016/j.apcatb.2016.12.014
0926-3373/

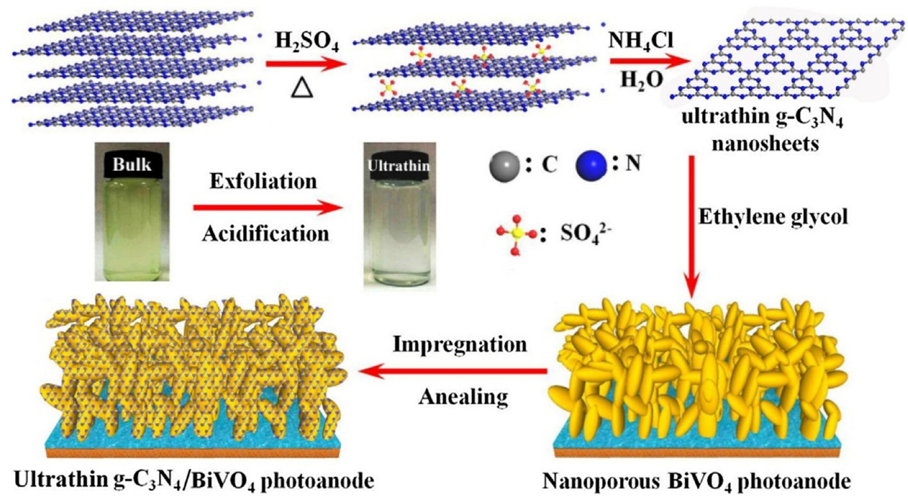

Scheme 1. Schematic illustration of the exfoliation and acidification process for fabricating ultrathin g-C_3N_4 nanosheets and $BiVO_4$/g-C_3N_4-NS photoanodes.

like layered structure with weak van der Waals force. More recently, both theoretical and experimental studies demonstrated that g-C_3N_4 possesses a unique thickness-dependent bandgap, and ultrathin thick 2D nanosheets can effectively enlarge the bandgap with respect to bulk materials, which is attributed to the well-known quantum confinement effect by shifting the conduction and valence band edges in opposite directions [33,34,37–39]. Moreover, owning to the ultrathin layered structure, the g-C_3N_4 nanosheets demonstrated impressive carrier mobility and were extensively applied in various electronic and optoelectronic devices [40]. Thereby, reducing the bulk 3D g-C_3N_4 into ultrathin 2D nanosheets and coating on photoanodes as co-catalysts may not only facilitate the rapid hole transfer from their contact interfaces, but also enhance the oxygen oxidation capability due to the enlarged valence band.

Herein, we demonstrate a simple ethylene glycol dispersion and impregnation method for uniform coating ultrathin g-C_3N_4 nanosheets (g-C_3N_4-NS) on nanoporous $BiVO_4$ photoanodes. More specifically, ultrathin g-C_3N_4-NS could effectively suppress the surface charge recombination on the $BiVO_4$, and photogenerated holes could be effectively stored on their valence band for water oxidation. Nyquist curves further demonstrated that the ultrathin g-C_3N_4 structure could greatly increase the charge-carrier density and facilitate more efficient electron-hole separation. As expected, the ultrathin g-C_3N_4-NS loading $BiVO_4$ photoelectrodes exhibit superior photoelectrochemical water oxidation in terms of onset potential, photocurrent density and H_2 generation capability as compared with pure as well as metal electrocatalysts modified $BiVO_4$ electrodes.

2. Results and discussion

Scheme 1 shows the synthesis process of ultrathin g-C_3N_4 –NS as well as their coating on nanoporous $BiVO_4$ photoanodes in this work. Briefly, ultrathin g-C_3N_4-NS was prepared by an acidification oxidation and exfoliation process for bulk g-C_3N_4, and finally dispersed in ethylene glycol solvent [41,42], which is crucial for the subsequent loading on nanoporous $BiVO_4$ photoanodes. The X-ray diffraction pattern of g-C_3N_4-NS (Fig. S1B) is consistent with the bulk g-C_3N_4, suggesting that the nanosheets basically possess the same crystal structure as the bulk g-C_3N_4. With respect to the bulk g-C_3N_4, the peak originated from the periodic stacking of layers in the nanosheets is shifted from 27.34° to 27.98°, indicating a decreased gallery distance between the nanosheets [27,28]. The UV–vis absorption spectrum of g-C_3N_4-NS (Fig. S2A) clearly shows an obvious blue shift of the intrinsic absorption edge with respect to the bulk g-C_3N_4. The derived bandgap from the plot versus the energy of the absorbed light (Fig. S2B) is 3.03 eV for the ultrathin nanosheets, which is larger than the bulk material of 2.75 eV. The band structure of g-C_3N_4 and pure $BiVO_4$ has been tested and calculated. Besides, the band structure of the heterostructure has been shown in Fig. S3.

Fig. 1A shows the typical transmission electron microscope (TEM) image of the $BiVO_4$/g-C_3N_4-NS sample. The nanoporous $BiVO_4$ photoanodes have been coated by ultrathin g-C_3N_4 nanolayers, and no evident bulk structure as a result of self-agglomeration have been observed. The high resolution TEM image in Fig. 1B exhibits that ultrathin g-C_3N_4 nanolayers with a thickness of 2 nm have been compactly attached on the surfaces of monoclinic $BiVO_4$ nanocrystals. Moreover, both carbon and nitrogen elements were detected in the whole regions from the elemental mapping images (Fig. 1C) and elemental line scanning (Fig. S4), which confirm the uniform dispersion of a g-C_3N_4 nanolayers on the surfaces of nanoporous $BiVO_4$. However, as compared with pure nanoporous $BiVO_4$ sample as shown in Fig. S5, the SEM images (Fig. 1D and E) and XRD patterns (Fig. 1F) demonstrated no evident crystals structure or morphology change, which should be due to the uniform dispersion and ultrathin thickness of g-C_3N_4 nanosheets. Besides, the fourier transform infrared (FT-IR) spectra have also been performed. As shown in Fig. S6, the basic peaks of g-C_3N_4 have been clearly observed in the as-prepared samples [29,33], The UV–vis diffuse reflectance spectra (DRS) were utilized to investigate the band gap energy (E_g) values of the crystals (Fig. S2). As a result of large direct bandgap energy (3.03 eV) of ultrathin g-C_3N_4-NS, the absorption edge and intensity of $BiVO_4$/g-C_3N_4-NS are generally consistent with pure $BiVO_4$ with direct band gap energy (E_g) of 2.48 eV. On the basis of above results, it can be confirmed that ultrathin C_3N_4 nanosheets could be successfully and uniformly coated on the $BiVO_4$ photoanodes by this simple impregnation process.

Fig. 2 shows the high-resolution C1 s and N1 s spectra of g-C_3N_4-NS and $BiVO_4$/g-C_3N_4-NS. The C1 s spectra (Fig. 2A) shows two deconvoluted peaks at 288.6 eV and 284.8 eV, ascribed to the signals of sp^2-bonded carbon (N—C=N) and standard reference carbon, which is usually observed in the XPS spectrum of carbon nitrides. In Fig. 2B, the high resolution N1 s spectra can be also deconvoluted into three different peaks. The N1 s peak at 398.9 eV corresponds to sp^2 hybridized aromatic N bonded to carbon atoms (C=N—C). The peak at 399.7 eV is assigned to the tertiary N bonded to carbon

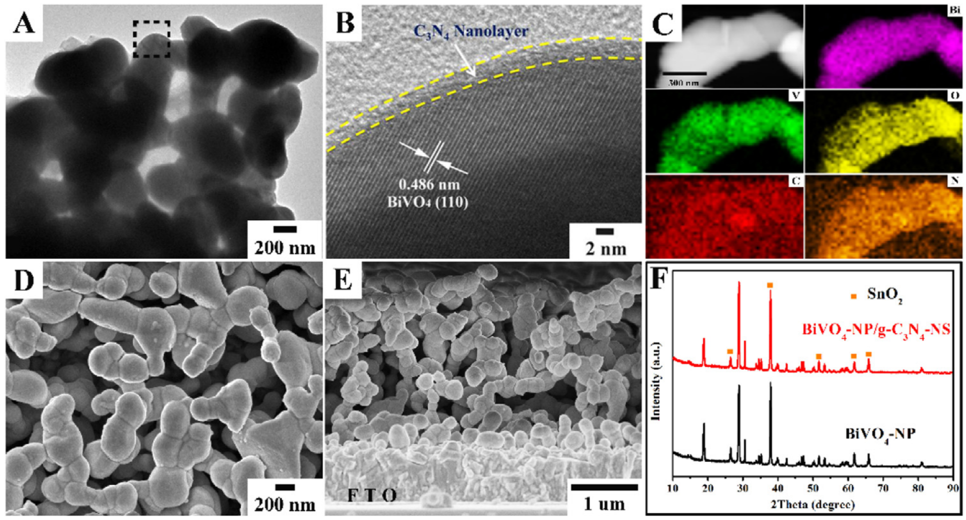

Fig. 1. TEM (A), HRTEM (B) and the corresponding elemental mappings (C) images of $BiVO_4$/g-C_3N_4-NS. The image in (A) is taken from the region marked with a rectangle in (B). Finally, top (D) and side view (E) SEM images, XRD (F) patterns of $BiVO_4$/g-C_3N_4-NS.

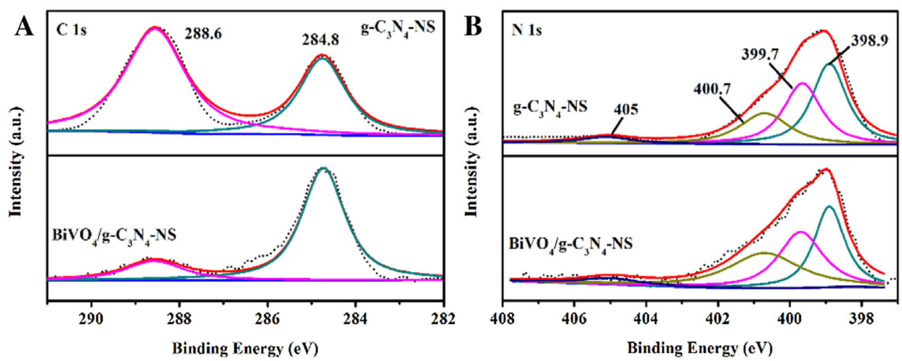

Fig. 2. XPS spectra of g-C_3N_4-NS and $BiVO_4$/g-C_3N_4-NS: (A) C 1s, (b) N 1s.

atoms in the form of N–(C)$_3$ or H—N–(C)$_2$. The peak with a high binding energy at 400.7 eV is attributed to quaternary N bonded to three carbon atoms in the aromatic cycles [43,44]. And the very weak peak at 405 eV corresponds to the π excitations [45,46]. Combing with the above results, except for the peaks intensity, the bonding characteristics of C1 s and N1 s have no apparent change between g-C_3N_4-NS and $BiVO_4$/g-C_3N_4-NS photoanodes.

Fig. 3 shows the typical current-potential curves of $BiVO_4$, $BiVO_4$/g-C_3N_4-NS, and $BiVO_4$/bulk g-C_3N_4 under visible light ($\lambda \geq 420$ nm) in 0.1 M Na_2SO_4 electrolyte. The $BiVO_4$/g-C_3N_4-NS provides a photocurrent density of 3.12 mA/cm^{-2} at 1.23 V vs. RHE, which is about 7 and 4 times higher than those of $BiVO_4$ (0.45 mA/cm^{-2} at 1.23 V vs. RHE) and $BiVO_4$/bulk g-C_3N_4 (0.76 mA/cm^{-2} at 1.23 V vs. RHE), respectively. The enhanced photocurrent density of $BiVO_4$/g-C_3N_4-NS photoanode can be attributed to the efficient charge separation as well as holes transfer between $BiVO_4$ and g-C_3N_4-NS. However, for the bulk g-C_3N_4, the direct charge transfer across bulk layers are very difficult, the photogenerated holes from $BiVO_4$ would accumulate on their contact interfaces, exhibiting poor surface reaction kinetics for water oxidation. Furthermore, the traditional metal cocatalysts modified $BiVO_4$ photoanodes have also been prepared according to the previous reports, and compared with the ultrathin g-C_3N_4-NS loaded $BiVO_4$ photoanode under the same conditions. In the case of CoPi and FeOOH, the photocurrent densities of $BiVO_4$ photoanodes could be increased up to 1.4 and 1.17 mA/cm^2 at 1.23 V vs. RHE, respectively, which are much lower than that of $BiVO_4$/g-C_3N_4-NS photoanode (3.12 mA/cm^2). Fig. 3B shows transient photocurrent response (1.23 V vs. RHE), and we can see that photocurrent densities of $BiVO_4$/CoPi or FeOOH photoanodes also do not drop or rise dramatically within 200 s, and basically in line with the values of Fig. 3A under the same bias. In addition, the water oxidation kinetics at the interface of the photo-anode/electrolyte was evaluated by electrochemical impedance spectroscopy (EIS) as shown in Fig. 3C [8,22], indicating that a fast charge separation and transfer have occurred in the interfaces between $BiVO_4$ and g-C_3N_4-NS. According to the previous reports [47,48], two equivalent circuit shown in Fig. S7 are used to fit EIS curves of $BiVO_4$ and $BiVO_4$/g-C_3N_4-NS, respectively. Fig. 3D shows hydrogen evolution versus time at the Pt counter electrode for these different photoanodes. The maximum amount of the H_2 generated by the $BiVO_4$/g-C_3N_4 NS was 121.33 μmol after 150 min. On the contrary, the CoPi, FeOOH and bulk g-C_3N_4 loaded $BiVO_4$ as well as pure $BiVO_4$ only produce trace amounts of H_2 (51.29, 42.56, 25.97, and 11.56 μmol) under the same conditions.

On the basis of above results, a possible mechanism for clarifying the charge transfer on $BiVO_4$/g-C_3N_4-NS has been illustrated in Scheme 2. As a result of the large bandgap (E_g = 3.03 eV) of ultrathin g-C_3N_4-NS, only the $BiVO_4$ could be excited under visible light irradiation, and the photogenerated electrons and holes are formed on the conduction band and valance band, respectively. In the $BiVO_4$/g-C_3N_4-NS, due to the staggered energy band and superior structure, the photogenerated electrons favorably transfer from the conduction band of $BiVO_4$ to FTO along the nanoporous structure, which

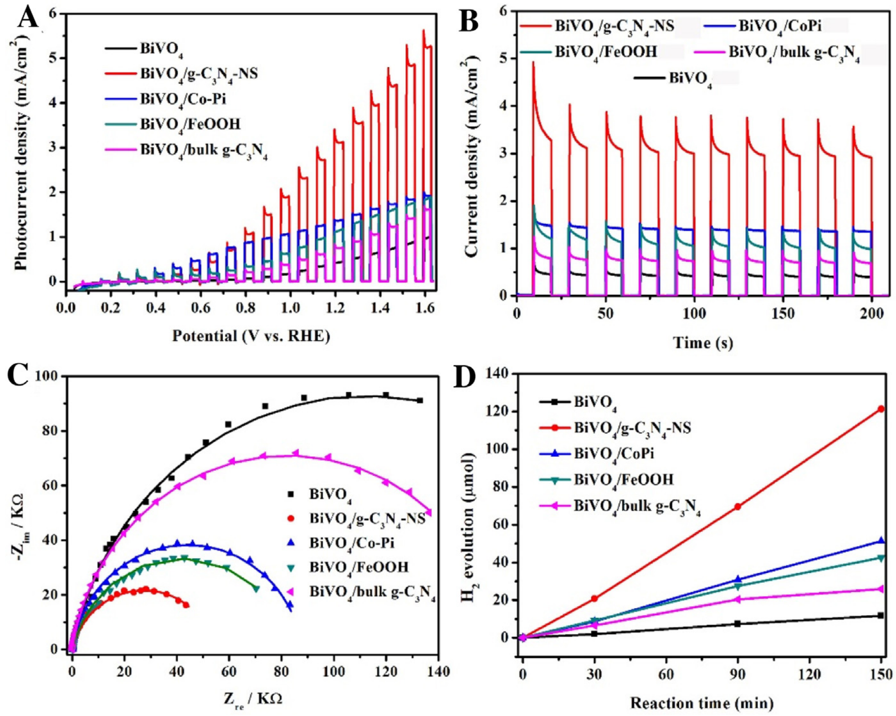

Fig. 3. (A) J-V curves, (B) transient photocurrent response (1.23 V vs. RHE), (C) electrochemical impedance spectroscopy (EIS, solid line is a curve after fitting) and (D) H_2 production for different photoanodes measured with visible-light illumination (λ > 420 nm) in 0.1 M Na_2SO_4.

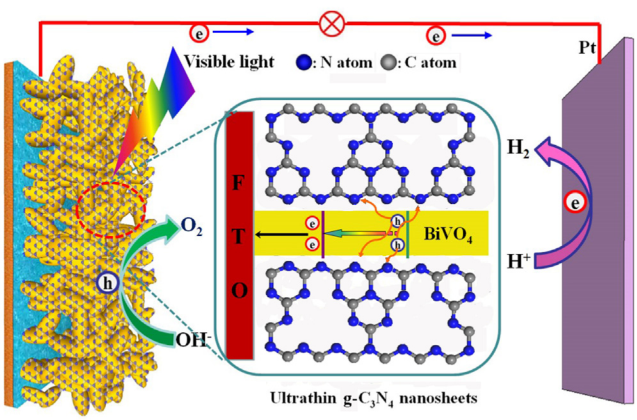

Scheme 2. Schematic illustration of the charge transfer in $BiVO_4$/g-C_3N_4-NS photoanodes.

shorten the travel distance of electron transport and reduce the chance of recombination. Then, the photogenerated electrons move to the Pt electrode via external circuit and reducing water to generate hydrogen. At the same time, the photogenerated holes are transferred from the valence band of $BiVO_4$ to the valence band of g-C_3N_4-NS, and accumulating in the surface of g-C_3N_4-NS for water oxidation. Notably, the integration of nanoporous and ultrathin film structures possesses short travel distance for photogenerated electron-hole pairs, which contribute to the high PEC activity for water oxidation, and provide enough surface active sites for PEC water oxidation.

3. Conclusion

In summary, we have demonstrated a flexible strategy for rationally constructing ultrathin g-C_3N_4 nanosheets on the surfaces of nanoporous $BiVO_4$ photoanodes. The ultrathin $BiVO_4$/g-C_3N_4-NS photoanode exhibits a high photocurrent density of 3.12 mA/cm^{-2} at 1.23 V vs. RHE for water oxidation and H_2 generation capability under visible light (λ ≥ 420 nm) irradiation. The improvement in PEC performance can be attributed to the g-C_3N_4-NS serving as an efficient metal-free cocatalyst owing to its enlarged bandgap (3.03 eV). The ultrathin g-C_3N_4-NS thus effectively promotes the efficient charge separation and holes migration on the ultrathin g-C_3N_4 nanolayer, suppressing the interfacial charge recombination. This work provides an efficient strategy for constructing metal-free cocatalyst on semiconductor photoanodes for improving the PEC activity.

Acknowledgment

This work was supported by the “Hundred Talents Program” of the Chinese Academy of Science and the National Natural Science Foundation of China (21622310, 21573264, 21273255, 21303232).

Appendix A. Supplementary data

Supplementary data associated with this article can be found, in the online version, at http://dx.doi.org/10.1016/j.apcatb.2016.12.014.

References

[1] T. Hisatomi, J. Kubota, K. Domen, Chem. Soc. Rev. 43 (2014) 7520–7535.
[2] T. Wang, Z.B. Luo, C.C. Li, J.L. Gong, Chem. Soc. Rev. 43 (2014) 7469–7484.
[3] M.G. Walter, E.L. Warren, J.R. McKone, S.W. Boettcher, Q. Mi, E.A. Santori, N.S. Lewis, Chem. Rev. 110 (2010) 6446–6473.
[4] H.J. Yu, R. Shi, Y.F. Zhao, Geoffrey I.N. Waterhouse, L.Z. Wu, C.H. Tung, T.R. Zhang, Adv. Mater. 28 (2016) 9454–9477.
[5] Y. Park, K.J. McDonald, K.S. Choi, Chem. Soc. Rev. 42 (2013) 2321–2337.
[6] S. Tokunaga, H. Kato, A. Kudo, Chem. Mater. 13 (2001) 4624–4628.
[7] F.F. Abdi, L. Han, A.H.M. Smets, M. Zeman, B. Dam, R. van de Krol, Nat. Commun. 4 (2013) 2195–2201.
[8] W.J. Luo, Z.S. Yang, Z.S. Li, J.Y. Zhang, J.G. Liu, Z.Y. Zhao, Z.Q. Wang, S.C. Yan, T. Yu, Z.G. Zou, Energy Environ. Sci 4 (2011) 4046–4051.
[9] K.J. McDonald, K.S. Choi, Energy Environ. Sci. 5 (2012) 8553–8557.

[10] J.A. Seabold, K.S. Choi, J. Am. Chem. Soc. 134 (2012) 2186–2192.
[11] T.W. Kim, K.S. Choi, Science 343 (2014) 990–994.
[12] X. Zhao, W.J. Luo, J.Y. Feng, M.X. Li, Z.S. Li, T. Yu, Z.G. Zou, Adv. Energy Mater. 4 (2014) 1301785.
[13] C.C. Feng, Z.B. Jiao, S.P. Li, Y. Zhang, Y.P. Bi, Nanoscale 7 (2015) 20374.
[14] S.K. Pilli, T.E. Furtak, L.D. Brown, T.G. Deutsch, J.A. Turner, A.M. Herring, Energy Environ. Sci. 4 (2011) 5028–5034.
[15] D.K. Zhong, S.J. Choi, D.R. Gamelin, J. Am. Chem. Soc. 133 (2011) 18370–18377.
[16] A.J.E. Rettie, H.C. Lee, L.G. Marshall, J.F. Lin, C. Capan, J. Lindemuth, J.S. McCloy, J.S. Zhou, A.J. Bard, C.B. Mullins, J. Am. Chem. Soc. 135 (2013) 11389–11396.
[17] M. Zhou, J. Bao, Y. Xu, J.J. Zhang, J.F. Xie, M.L. Guan, C.L. Wang, L.Y. Wen, Y. Lei, Y. Xie, ACS. Nano 8 (2014) 7088–7098.
[18] M. Ma, J.K. Kim, K. Zhang, X. Shi, S.J. Kim, J.H. Moon, J.H. Park, Chem. Mater 26 (2014) 5592–5597.
[19] X. Shi, Y. Choi, K. Zhang, J. Kwon, D.Y. Kim, J.K. Lee, S. Ho Oh, J.K. Kim, J.H. Park, Nat. Commun. 5 (2014) 4775.
[20] P.M. Rao, L.L. Cai, C. Liu, I.S. Cho, C.H. Lee, J.M. Weisse, P.D. Yang, X.L. Zheng, Nano Lett. 14 (2014) 1099–1105.
[21] J.Z. Su, L.J. Guo, N.Z. Bao, C.A. Grimes, Nano Lett. 11 (2011) 1928–1933.
[22] X.X. Chang, T. Wang, P. Zhang, J.J. Zhang, A. Li, J.L. Gong, J. Am. Chem. Soc. 137 (2015) 8356–8359.
[23] M. Zhong, T. Hisatomi, Y. Kuang, J. Zhao, M. Liu, A. Iwase, Q.J. Jia, H. Nishiyama, T. Minegishi, M. Nakabayashi, N. Shibata, R. Niishiro, C. Katayama, H. Shibano, M. Katayama, A. Kudo, T. Yamada, K. Domen, J. Am. Chem. Soc. 137 (2015) 5053–5060.
[24] Y.F. Zhao, X.D. Jia, G.B. Chen, L. Shang, Geoffrey I.N. Waterhouse, L.Z. Wu, C.H. Tung, D. O'Hare, T.R. Zhang, J. Am. Chem. Soc. 138 (2016) 6517–6524.
[25] Y.F. Zhao, B. Zhao, J.J. Liu, G.B. Chen, R. Gao, S.Y. Yao, M.Z. Li, Q.H. Zhang, L. Gu, J.L. Xie, X.D. Wen, L.Z. Wu, C.H. Tung, D. Ma, T.R. Zhang, Angew. Chem. Int. Ed. 55 (2016) 4215–4219.
[26] J. Liu, Y. Liu, N.Y. Liu, Y.Z. Han, X. Zhang, H. Huang, Y. Lifshitz, S.T. g Lee, J. Zhong, Z.H. Kang, Science 347 (2015) 6225.
[27] X.C. Wang, K. Maeda, A. Thomas, K. Takanabe, G. Xin, J.M. Carlsson, K. Domen, M. Antonietti, Nat. Mater. 8 (2009) 76–80.
[28] L. Ge, F. Zuo, J.K. Liu, Q. Ma, C. Wang, D.Z. Sun, L. Bartels, P.Y. Feng, J. Phys. Chem. C 116 (2012) 13708–13714.
[29] D.D. Zheng, C.Y. Pang, Y.X. Liu, X.C. Wang, Chem. Commun. 51 (2015) 9706–9709.
[30] H.X. Zhao, H.T. Yu, X. Quan, S. Chen, Y.B. Zhang, H.M. Zhao, H. Wang, App. Catal. B 152–153 (2014) 46–50.
[31] P. Niu, L. Zhang, G. Liu, H.M. Cheng, Adv. Funct. Mater. 22 (2012) 4763–4770.
[32] S.B. Yang, Y.J. Gong, J.S. Zhang, L. Zhan, L.L. Ma, Z.Y. Fang, R. Vajtai, X.C. Wang, P.M. Ajayan, Adv. Mater. 25 (2013) 2452–2456.
[33] J. Xu, L.W. Zhang, R. Shi, Y.F. Zhu, J. Mater. Chem. A 1 (2013) 14766–14772.
[34] L.C. Chen, X.T. Zeng, P. Si, Y.M. Chen, Y.W. Chi, D.H. Kim, G.N. Chen, Anal. Chem. 86 (2014) 4188–4195.
[35] J.L. Zhang, Z.W. Zhu, J.W. Di, Y.M. Long, W.F. Li, Y.F. Tua, Electrochim. Acta 186 (2015) 192–200.
[36] X.D. Zhang, X. Xie, H. Wang, J.J. Zhang, B.C. Pan, Y. Xie, J. Am. Chem. Soc. 135 (2013) 18–21.
[37] J.S. Zhang, Y. Chen, X.C. Wang, Energy Environ. Sci. 8 (2015) 3092–3108.
[38] Y.J. Zhang, T. Mori, L. Niu, J.H. Ye, Energy Environ. Sci. 4 (2011) 4517–4521.
[39] C.J. Li, S.P. Wang, T. Wang, Y.J. Wei, P. Zhang, J.L. Gong, Small 10 (2014) 2783–2790.
[40] Y. Hou, F. Zuo, A.P. Dagg, J.K. Liu, P.Y. Feng, Adv. Mater. 26 (2014) 5043–5049.
[41] X.R. Du, G.J. Zou, Z.H. Wang, X.L. Wang, Nanoscale 7 (2015) 8701–8706.
[42] H.J. Yu, L. Shang, T. Bian, R. Shi, Geoffrey I.N. Waterhouse, Y.F. Zhao, C. Zhou, L.Z. Wu, C.H. Tung, T.R. Zhang, Adv. Mater 28 (2016) 5080–5086.
[43] V.N. Khabashesku, J.L. Zimmerman, J.L. Margrave, Chem. Mater 12 (2000) 3264–3270.
[44] T. Komatsu, T. Nakamura, J. Mater. Chem. 11 (2001) 474–478.
[45] Q.X. Guo, Y. Xie, X.J. Wang, S.Y. Zhang, T. Hou, S.C. Lv, Chem. Commun. 1 (2004) 26–27.
[46] A. Thomas, A. Fischer, F. Goettmann, M. Antonietti, J.-O. Müller, R. Schlögl, J.M. Carlsson, J. Mater. Chem. 18 (2008) 4893–4908.
[47] Z.F. Hu, G. Liu, X.Q. Chen, Z.R. Shen, J.C. Yu, Adv. Funct. Mater. 26 (2016) 4445–4455.
[48] Z.F. Hu, Z.R. Shen, J.C. Yu, Chem. Mater 28 (2016) 564–572.